Atmospheric
Measurement
Techniques
Discussions

Measurement of iodine species and sulfuric acid using bromide chemical ionization mass spectrometers

Mingyi Wang[1,2*], Xu-Cheng He[3*#], Henning Finkenzeller[4], Siddharth Iyer[3], Dexian Chen[1,5], Jiali Shen[3], Mario Simon[6], Victoria Hofbauer[1,2], Jasper Kirkby[6,7], Joachim Curtius[6], Norbert Maier[8], Theo Kurtén[3,8], Douglas R. Worsnop[3,9], Markku Kulmala[3,10,11,12], Matti Rissanen[3,13], Rainer Volkamer[4], Yee Jun Tham[3#], Neil M. Donahue[1,2,5,14], and Mikko Sipilä[3]

[1]Center for Atmospheric Particle Studies, Carnegie Mellon University, Pittsburgh, PA, 15213, USA
[2]Department of Chemistry, Carnegie Mellon University, Pittsburgh, PA, 15213, USA
[3]Institute for Atmospheric and Earth System Research (INAR), University of Helsinki, 00014 Helsinki, Finland
[4]Department of Chemistry & CIRES, University of Colorado Boulder, Boulder, CO 80309, USA
[5]Department of Chemical Engineering, Carnegie Mellon University, Pittsburgh, PA, 15213, USA
[6]Institute for Atmospheric and Environmental Sciences, Goethe University Frankfurt, 60438 Frankfurt am Main, Germany
[7]CERN, the European Organization for Nuclear Research, CH-1211 Geneve 23, Switzerland
[8]Department of Chemistry, University of Helsinki, 00014 Helsinki, Finland
[9]Aerodyne Research, Inc., Billerica, MA, 01821, USA
[10]Helsinki Institute of Physics, P.O. Box 64 (Gustaf Hallstromin katu 2), FI-00014 University of Helsinki, Finland
[11]Joint International Research Laboratory of Atmospheric and Earth System Sciences, Nanjing University, Nanjing, China
[12]Aerosol and Haze Laboratory, Beijing Advanced Innovation Center for Soft Matter Science and Engineering, Beijing University of Chemical Technology, Beijing, China
[13]Aerosol Physics Laboratory, Physics Unit, Faculty of Engineering and Natural Sciences, Tampere University, Tampere, Finland
[14]Department of Engineering and Public Policy, Carnegie Mellon University, Pittsburgh, PA, 15213, USA
*These authors contributed equally to this work

#Correspondence to:
Xu-Cheng He (xucheng.he@helsinki.fi) and Yee Jun Tham (yee.tham@helsinki.fi).

Abstract. Iodine species are important in the marine atmosphere for oxidation and new-particle formation. Understanding iodine chemistry and iodine new-particle formation requires high time resolution, high sensitivity, and simultaneous measurements of many iodine species. Here, we describe the application of bromide chemical ionization mass spectrometers (Br-CIMS) to this task. During iodine new-particle formation experiments in the Cosmics Leaving OUtdoor Droplets (CLOUD) chamber, we have measured gas-phase iodine species and sulfuric acid using two Br-CIMS, one coupled to a Multi-scheme chemical IONization inlet (Br-MION-CIMS) and the other to a Filter Inlet for Gasses and AEROsols inlet (Br-FIGAERO-CIMS). From offline calibrations and inter-comparisons with other instruments attached to the CLOUD chamber, we have quantified the sensitivities of the Br-MION-CIMS to HOI, I_2, and H_2SO_4 and obtain detection limits of 5.8×10^6, 6.3×10^5, and 2.0×10^5 molec cm^{-3}, respectively, for a 2-min integration time. From binding energy calculations, we estimate the detection limit for HIO_3 to be 1.2×10^5 molec cm^{-3}, based on an assumption of maximum sensitivity. Detection limits in the Br-FIGAERO-CIMS are around one order of magnitude higher than those in the Br-MION-CIMS; for example, the detection limits for HOI and HIO_3 are 3.3×10^7 and 5.1×10^6 molec cm^{-3}, respectively. Our comparisons of the performance of the MION inlet and the FIGAERO inlet

45 show that bromide chemical ionization mass spectrometers using either atmospheric pressure or reduced pressure
46 interfaces are well-matched to measuring iodine species and sulfuric acid in marine environments.

47

48 **1 Introduction**
49 Reactive iodine species are released into the atmosphere mainly by biological processes in marine environments (i.e.
50 from macro- and micro-algae) (McFiggans et al., 2004), O_3 deposition on the sea surface (Carpenter et al., 2013), as
51 well as from the sea ice (Spolaor et al., 2013) and snowpack in the polar region (Raso et al., 2017). Once emitted,
52 iodine species can modify atmospheric oxidative capacity via a chain of catalytic reactions with O_3 that form iodine
53 oxides, leading to about 20–28 % of O_3 loss in the marine boundary layer (Prados-Roman et al., 2015; Sherwen et al.,
54 2016). Through convection, reactive iodine species can be transported from the lower troposphere to the upper
55 troposphere-lower stratosphere, causing one third of the iodine-induced ozone loss in the upper troposphere-lower
56 stratosphere (Koenig et al., 2020). Another important effect of iodine species is their contribution to atmospheric new-
57 particle formation. O'Dowd et al. (O'Dowd et al., 2002) showed that particles are produced from condensable iodine-
58 containing vapours at a costal location (Mace Head in Ireland). Recent studies have demonstrated that iodic acid (HIO_3)
59 dominates the charged iodine cluster formation, and drives the bursts of freshly-formed particles in coastal regions
60 (He et al., 2020; Sipilä et al., 2016). This process thereby may enhance cloud condensation nuclei formation, affecting
61 climate both directly and indirectly (Saiz-Lopez et al., 2012; Simpson et al., 2015).

62

63 Understanding iodine chemistry and iodine driven new-particle formation requires high time resolution, high
64 sensitivity, and simultaneous measurements of iodine species. However, this has been a long-standing challenge due
65 to their low abundance and short atmospheric lifetimes. Previous studies have achieved detection of relatively more
66 abundant molecular iodine (I_2), iodine monoxide (IO), and iodine dioxide (OIO) via optical spectroscopy, such as
67 differential optical absorption (Leigh et al., 2010), cavity ring-down (Bitter et al., 2005), cavity enhanced absorption
68 (Vaughan et al., 2008), laser-induced fluorescence (Dillon et al., 2006), and resonance fluorescence (Gómez Martín
69 et al., 2011). The spectroscopic techniques are invaluable; however, their very specificity limits them to the detection
70 of a few iodine compounds, and they are less sensitive to other iodine species that have congested or broad absorption
71 cross sections such as hypoiodous acid (HOI) and iodic acid (HIO_3).

72

73 Another commonly used technique is mass spectrometry; it has a fast response time and a low detection limit, but
74 extra calibration efforts are needed for the quantification of the detection sensitivity. For example, photoionization
75 (Gómez Martín et al., 2013) and chemical ionization mass spectrometry (CIMS) have been employed to detect a suite
76 of halogen species. Reagent ions used with CIMS include: SF_5^- for HCl and $ClONO_2$ (Marcy et al., 2004); iodide (I^-)
77 for atmospheric chlorine and bromine species such as $ClNO_2$, Cl_2, ClO, BrO, and BrCl (Kercher et al., 2009; Lee et
78 al., 2018; Tham et al., 2016); superoxide (O_2^-) for molecular iodine (I_2) (Finley and Saltzman, 2008); and both nitrate
79 (NO_3^-) (Sipilä et al., 2016) and protonated water (H_3O^+) (Pfeifer et al., 2020) for HIO_3. The nitrate-CIMS and H_3O^+-
80 CIMS suffer from the limited analyte affinity to the reagent ions. The iodide-CIMS can effectively measure chlorine
81 and bromine species, but it is not suitable to detect iodine species due to the ambiguity in peak identification.

Atmospheric
Measurement
Techniques
Discussions

82

83   Bromide ion (Br⁻) exhibits an affinity to a wide spectrum of iodine containing species. Br-CIMS has been routinely

84   used to measure chlorine species (Lawler et al., 2011), HO_2 radicals (Sanchez et al., 2016), organic vapors and sulfuric

85   acid (Rissanen et al., 2019), and nitric acid (Wang et al., 2020). Like chlorine species, iodine species are known to

86   cluster with bromide ions via halogen (or hydrogen) bonds; as such, here we explore using the Br-CIMS to measure

87   gas-phase iodine species and sulfuric acid simultaneously at concentrations relavant to the marine boundary layer. In

88   this study, we demonstrate the detection of various gas-phase inorganic iodine species with the Br-CIMS and explore

89   the effect of relative humidity (RH) on that detection. We then quantify the sensitivies of several gas-phase halogen

90   species via inter-method calibration, offline calibration, and quantum chemical calculations. Finally, we compare the

91   performance of Br-MION-CIMS and Br-FIGAERO-CIMS and show that both of them are well-suited for iodine

92   species measurement in the atmosphere.

93

94   **2 Methodology**

95   **2.1 The CLOUD facility**

96   We conducted measurements and instrument inter-comparison at the CERN CLOUD facility, a 26.1 m³

97   electropolished stainless-steel chamber that enables new-particle formation experiments simulating the typical range

98   of tropospheric conditions with scrupulous cleanliness and minimal contamination (Duplissy et al., 2016; Kirkby et

99   al., 2011). The CLOUD chamber is mounted in a thermal housing, capable of keeping temperature constant in a range

100 of -65 °C and +100 °C with ±0.1 °C precision (Dias et al., 2017) and relative humidity commonly between < 0.5%

101 and 80%. Photochemical processes are driven by different light sources, including four 200 W Hamamatsu Hg-Xe

102 lamps with significant spectral irradiance between 250 and 450 nm, and an array of 48 green light LEDs at 528 nm

103 with adjustable optical power up to 153 W. Ion-induced nucleation under different ionization levels is simulated with

104 a combination of electric fields (electrodes at ±30 kV at top and bottom of the chamber) which can be turned on to

105 rapidly scavenge smaller ions, and a high-flux beam of 3.6 GeV pions (π^+) which enhances ion production when turned

106 on. Mixing is accelerated with magnetically coupled fans mounted at the top and bottom of the chamber. The

107 characteristic gas mixing time in the chamber during experiments is a few minutes. The loss rate of condensable vapors

108 onto the chamber wall is comparable to the condensation sink in pristine boundary layer environments (e.g. 2.2×10^{-3}

109 s^{-1} for H_2SO_4 at 5 °C). To avoid a memory effect between different experiments, the chamber is periodically cleaned

110 by rinsing the walls with ultra-pure water and heating to 100 °C for at least 24 hours, ensuring extremely low

111 contaminant levels of sulfuric acid ($< 5 \times 10^4$ cm⁻³) and total organics (< 150 pptv) (Kirkby et al., 2016; Schnitzhofer

112 et al., 2014). The CLOUD gas system is also built to the highest technical standards of cleanliness and performance.

113 The dry air supply for the chamber is provided by cryogenic oxygen (Messer, 99.999 %) and cryogenic nitrogen

114 (Messer, 99.999 %) mixed at the atmospheric ratio of 79:21. Ultrapure water vapor, ozone and other trace gases can

115 be precisely added to attain mixing ratios at different levels.

116

117 **2.2 Br-MION-CIMS**

118   We measured gas-phase iodine species with a bromide chemical ionization atmospheric pressure interface time-of-
119   flight mass spectrometer (Junninen et al., 2010) coupled with a Multi-scheme chemical IONization inlet (Br-MION-
120   CIMS) (Rissanen et al., 2019). The Br-MION inlet consists of an electrically grounded 24 mm inner diameter stainless
121   steel flow tube, attached to an ion source. For the CLOUD measurements, the length of the sampling inlet was ~1.5
122   m and was designed to be in a laminar flow with a fixed total flow rate of 20 standard liters per minute (slpm). An ion
123   filter, operated with positive and negative voltage, was placed at the front of the inlet to filter out any ions in the
124   sample air prior to ion-molecule reaction chamber in the inlet. The reagent ions, bromide (Br^-) and the bromide-water
125   cluster ($H_2O \cdot Br^-$), were produced by feeding 25 standard milliliters per minute (mlpm) of nitrogen (N_2) flow through
126   a saturator containing dibromomethane (CH_2Br_2; > 99.0 %, Tokyo Chemical Industry) into the ion source, where the
127   reagent was ionized by soft X-ray radiation. The resulting ions were then accelerated by a 2500 V ion accelerator array
128   and focused by a 250 V ion deflector into the laminar sampling flow of the inlet via a 5 mm orifice. A small counter
129   flow (~40 mlpm) was applied through the orifice to prevent any mixing of the electrically neutral reagent vapor with
130   the sampling flow. The details of the inlet design, setup, and operation are described in Rissanen et al., 2019.

131

132   **2.3 Br-FIGAERO-CIMS**

133   We also measured both the gas- and particle-phase compositions via thermal desorption using a bromide chemical
134   ionization time-of-flight mass spectrometer equipped with a Filter Inlet for Gases and AEROsols (Br-FIGAERO-
135   CIMS) (Lopez-Hilfiker et al., 2014). FIGAERO is a manifold inlet for a CIMS with two operating modes. In the
136   sampling mode, gases are directly sampled into a 150 mbar ion-molecule reactor, using coaxial core sampling to
137   minimize their wall losses in the sampling line. The total flow is maintained at 18.0 slpm and the core flow at 4.5 slpm;
138   the CIMS samples at the center of the core flow with a flow rate at ~1.6 slpm. Concurrently, particles are collected on
139   a PTFE filter via a separate dedicated port with a flow rate of 6 slpm. In the desorption mode, the filter is automatically
140   moved into a pure N_2 gas stream flowing into the ion molecule reactor, while the N_2 is progressively heated upstream
141   of the filter to evaporate the particles via temperature programmed desorption. Analytes are then chemically ionized
142   by Br^- and extracted into a mass spectrometer.

143

144   **2.4 CE-DOAS**

145   For the quantitative measurement of gas-phase molecular iodine (I_2), we deployed a Cavity Enhanced Differential
146   Optical Absorption Spectroscopy instrument (CE-DOAS) (Meinen et al., 2010). CE-DOAS determines concentrations
147   of trace gases from the strength of differential spectral features in a reference spectrum. The accuracy of the method
148   is ultimately determined by the uncertainty of the respective absorption cross sections. It is thus an absolute method
149   and does not depend on an instrument specific detection efficiency. To maximize the measurement sensitivity towards
150   I_2, we used a setup optimized for the green wavelength range (508-554 nm), where I_2 exhibits strong differential
151   absorption features. The measurement light is provided by a green light emitting diode (LED Engin). Spectral
152   dispersion is established with a Czerny-Turner grating spectrometer (Princeton Instruments Acton 150), resulting in
153   an optical resolution of 0.73 nm full width at half maximum at 546 nm. Intensities are monitored with a CCD detector
154   (charge-coupled device, Princeton Instruments PIXIS400B) cooled to -70 °C. Highly reflective mirrors (Advanced

155   Thin Films) enhance the 1 m mirror separation to an effective optical path length of 15-23 km. The effective spectral

156   mirror reflectivity was established by comparing light intensity spectra in the presence of N_2 and He (Washenfelder

157   et al., 2008). The abundance of trace gases is then determined by comparing spectra of chamber air relative to reference

158   spectra recorded with ultrapure N_2 without I_2. Chamber air is drawn into the cavity with a constant flow rate of 1 slpm.

159   Variations of the sampling flow did not result in changes in measured I_2 concentrations, indicating that photolysis

160   from the measurement light within the instrument was negligible. The following absorbers were included in the fit: I_2

161   (Spietz et al., 2006), NO_2 (Vandaele et al., 1998), H_2O (Rothman et al., 2010), O_2-O_2 collision-induced absorption

162   (Thalman and Volkamer, 2013), and a polynomial of sixth order. The setup allowed a 1-minute detection limit of 25

163   pptv, or 8 pptv for integration times of 10 minutes, respectively. Periodic automated recordings of N_2 reference spectra

164   were recorded to ensure baseline stability. The optical path length at the time of measurement was continuously

165   confirmed for consistency by the measurement of the O_2-O_2 collision-induced absorption and H_2O column in the same

166   analysis window. The overall systematic accuracy for the I_2 time series is estimated to be 20 %, never better than the

167   detection limit, resulting from the uncertainty in cross sections and the stability of the baseline.

168

169   **2.5 Quantum chemical calculations**

170   We used quantum chemical calculations to estimate the cluster formation enthalpy of halogen containing species and

171   bromide ions. The initial conformer sampling was performed using the Spartan '14 program. The cluster geometry

172   was then optimized using density function theory methods at the ωB97X-D/aug-cc-pVTZ-PP level of theory (Chai

173   and Head-Gordon, 2008; Kendall et al., 1992). Iodine pseudopotential definitions were taken from the EMSL basis

174   set library (Feller, 1996). Calculations were carried out using the Gaussian 09 program (Frisch et al., 2010). An

175   additional coupled-cluster single-point energy correction was carried out on the lowest energy geometry to calculate

176   the final cluster formation enthalpy. The coupled-cluster calculation was performed at the DLPNO-CCSD(T)/def2-

177   QZVPP level using the ORCA program ver. 4.0.0.2 (Neese, 2012; Riplinger and Neese, 2013). In Table 1 we present

178   calculated cluster formation enthalpies based on the optimized geometries.

179

180   **3 Results and Discussion**

181   **3.1 Detection of gas-phase inorganic species by Br-MION-CIMS**

182   We show in Fig. 1 the selected inorganic species observed with the Br-MION-CIMS during an iodine new-particle

183   formation experiment in the CLOUD chamber. The peak identities are indicated in the labels. Observed species

184   include I_2 and its various oxidation products. There are also a few other halogen-containing inorganic species such as

185   Cl_2, ICl and IBr, likely coming from the impurities in the iodine source. Non-halogen inorganic species such as H_2SO_4

186   can also react with bromide ion and are detected. Due to the large negative mass defect of the bromine and iodine

187   atoms, and the high resolution (~10000 Th Th^{-1}) of the mass spectrometer, the peaks can be unambiguously

188   distinguished and identified in the mass spectrum. As shown in the lower panel of Fig. 1, most of the iodine-containing

189   species appear as a single peak in the unit mass range, except for $HIO_2 \cdot {}^{79}Br^-$ (m/z = 238.82), which overlaps with the

190   reagent ion cluster $({}^{79}Br_2 {}^{81}Br)^-$ (m/z = 238.75).

191
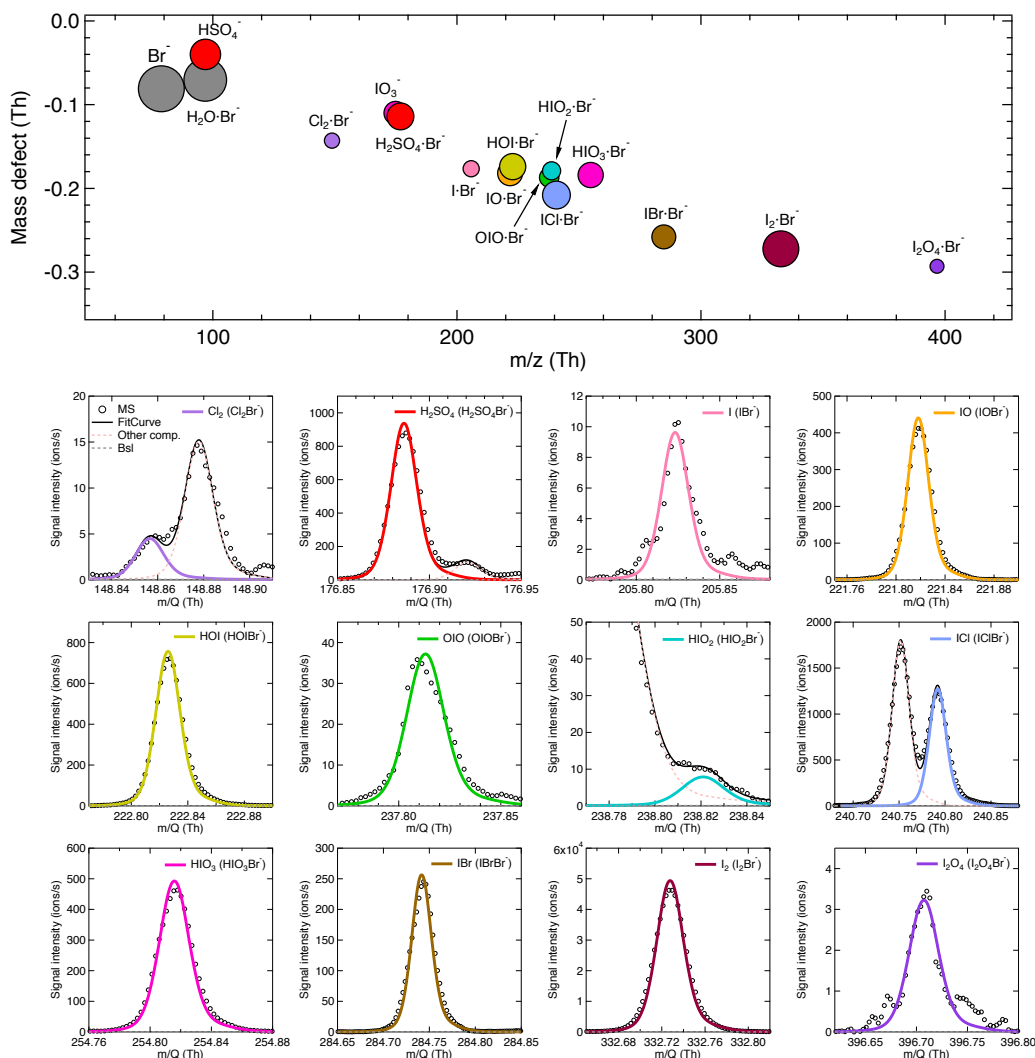
Figure 1. Gas-phase inorganic species measured with the Br-MION-CIMS. Mass defect (difference of exact mass to integer mass) versus m/z of gas-phase halogen species and sulfuric acid during an iodine new-particle formation experiment at 69 % relative humidity and -10 °C. Ions shown here are either clustered with or formed via proton transfer to a bromide ion. The area of the markers is proportional to the logarithm of the signal (counts per second). Shown in the lower panel are the high-resolution single peak fits for species in the mass defect plot in the upper panel.

The iodine new-particle formation experiments were conducted under experimental conditions typically found in the high-latitude marine boundary layer, with a temperature of -10 °C and a relative humidity of 69 %. As illustrated in Fig. 2, a typical experiment started with illumination of the chamber at constant I_2 (~60 pptv) using the green light to photolytically produce I atoms. The subsequent reactions of I and ~ 40 ppbv O_3 led to the formation of various oxidized iodine species within a few minutes. The most prominent species we observed from these experiments were IO, HOI and HIO_3, with lower but significant levels of OIO, HIO_2, and I_2O_4. Among these iodine oxides, IO rose the most

Atmospheric
Measurement
Techniques
Discussions
Open Access
EGU

205   rapidly; this is consistent with the first-generation production of IO from the I + O$_3$ reaction. After a few steps of

206   radical reactions, OIO, HIO$_2$ and HIO$_3$ reached steady state almost simultaneously. The only observed iodine oxide

207   dimer was I$_2$O$_4$ in this event, while I$_2$O$_2$, I$_2$O$_3$ and I$_2$O$_5$ were below the detection limit of both mass spectrometers. A

208   noticeable dip in the HIO$_3$ traces a few minutes after the onset of the reactions is likely due to the participation of HIO$_3$

209   in new-particle formation, resulting in an extra loss term and a lower steady-state concentration. When we turned off

210   the green light, the production of I radicals stopped and iodine species decayed.

211
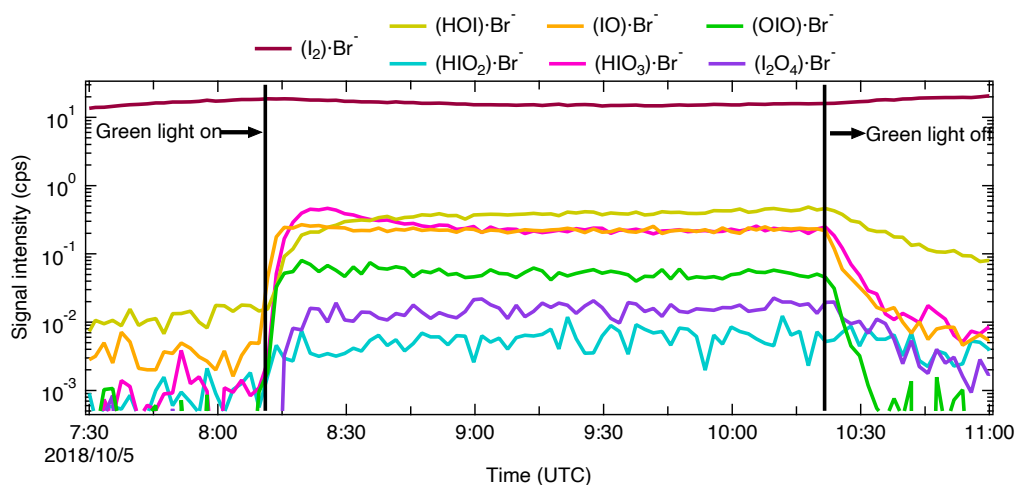
212
213   **Figure 2**. Evolution of selected iodine species during a typical run. The experiment was performed at 60 pptv I$_2$, 40 ppbv O$_3$, 69 %
214   relative humidity and -10 °C. The oxidized iodine species start to appear soon after switching on the green light at 08:11, 05 October
215   2018. The I atom production was halted at 10:21, 05 October 2018 by switching off the green light, and the concentration of
216   oxidized iodine species decayed away afterwards. All species are color-coded in the same way as in Fig. 1.
217

218   **3.2 Relative humidity dependence**

219   Water molecules can cluster with I$^-$ to form H$_2$O·I$^-$ in the iodide CIMS. This enhances the instrument sensitivities for

220   small molecules (i.e. inorganics) and reduces them for large molecules (i.e. organics) (Lee et al., 2014). To investigate

221   the role of water concentration in the sensitivity of the Br-MION-CIMS, we varied the relative humidity (RH) from

222   40 % to 80 % at a constant temperature of -10 °C. We show in Fig. 3 the correlation of I$_2$ time series from the Br-

223   MION-CIMS and the CE-DOAS throughout the experiment. During the RH transition, the ratio of the two reagent

224   ions, Br$^-$ and H$_2$O·Br$^-$, changed in the Br-MION-CIMS. As shown in Fig. 3 (a) and (b), using either reagent ion alone

225   for I$_2$ normalization results in discrepancies in recovered I$_2$ concentrations at different RH. However, if we use the

226   sum of these two reagent ions (Br$^-$ + H$_2$O·Br$^-$) for normalization, the humidity effect vanishes, as shown in the Fig. 3

227   (c). This suggests that the quantitative detection of I$_2$ molecules is robust and independent of RH, as long as a proper

228   normalization method is used for the Br-MION-CIMS. Furthermore, we have also carried out the HOI calibration and

229   used the same normalization method as described in section 3.3.4. During the calibration, we varied the water content

230   in the calibrator to vary OH concentrations. A good correlation between the modeled HOI concentrations and the

231   measured HOI signals also indicates that the different H$_2$O concentrations in the system do not affect the HOI detection.

232   This assertion may also be applicable to other molecules, but further confirmation is needed.

233
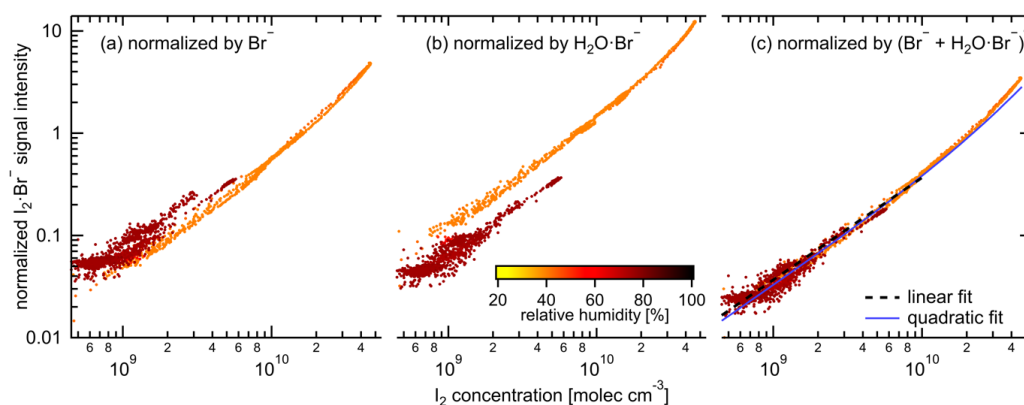
234
235 **Figure 3.** Signal normalization methods for the Br-MION-CIMS. The charger ions in the ion source of Br-MION-CIMS are Br^-
236 and $H_2O \cdot Br^-$ (both ^{79}Br and ^{81}Br). Their abundance depends both on the instrument tuning and the absolute humidity of the sampled
237 flow. The normalization of the $I_2 \cdot Br^-$ signal by only Br^- (a) or $H_2O \cdot Br^-$ (b) does not compensate for the humidity effect. Using the
238 sum of Br^- and $H_2O \cdot Br^-$ (c) for normalization yields a tight correlation to the true I_2 as measured by CE-DOAS, independent of the
239 humidity. The black dashed line and blue solid curve indicate the fitted linear and quadratic calibration curves, respectively.
240

241 **3.3 Quantification of gas-phase inorganic species**

242 **3.3.1 I_2 calibration using the CE-DOAS**

243 As shown in Fig. 3, we use the accurate I_2 time series measured with the CE-DOAS to calibrate normalized I_2 signals
244 in the Br-MION-CIMS. The I_2 concentrations used for the calibration span approximately 2 orders of magnitude,
245 reaching up to 4.6×10^{10} molec cm^{-3}. A linear fit, limited to I_2 concentrations smaller than 10^{10} molec cm^{-3}, establishes
246 the calibration factor $[I_2] = 2.7 \times 10^{10}$ molec $cm^{-3} \times I_2 \cdot {}^{79}Br^-/({}^{79}Br^- + H_2O \cdot {}^{79}Br^-)$. We also use a quadratic fit to establish
247 the calibration for the entire range of concentrations encountered during whole campaign (solid line in Fig. 3 (c)); two
248 curves agree well. The CE-DOAS I_2 detection limit is 6.3×10^8 molec cm^{-3} (25 pptv) for a 1 min integration time, and
249 the total systematic uncertainty is estimated to be 20%. Deviations between both time series are generally smaller than
250 10% (25 and 75 percentile 0.88 and 1.03, respectively). These small differences are consistent with incomplete
251 homogeneity of iodine concentrations in the chamber and the different sampling positions of CE-DOAS and Br-
252 MION-CIMS.

253

254 **3.3.2 I_2 calibration using a permeation tube**

255 We used an iodine permeation tube (VICI Metronic) as a source for offline calibration. The permeation tube was
256 encased within an electronically controlled heating mantle ($80 \sim 140$ (± 2) °C) to allow for adjustable yet steady iodine
257 permeation rates. The iodine permeation device was run continuously for at least 72 hours before any calibration
258 experiments to ensure that a complete equilibrium was reached in the system. We then confirmed the robustness of
259 the permeation device by the constant I_2 signal measured with Br-MION-CIMS for over 24 hours.

260

261 To determine the permeation rate of I_2, we trapped iodine in n-hexane at cryogenic temperatures in an all-glass
262 apparatus, following the method described in Chance et al. (Chance et al., 2010). We initially filled the absorption

263   glass vessel with 20 ml n-hexane (99.95%, Merck), and then weighed it to determine the combined mass. We then
264   immersed the absorption vessel into a wide-necked Dewar vessel, filled with an acetone/dry ice mixture (at $-80 \pm$
265   3 °C). After temperature equilibration, the I_2 molecules, carried by 50 mlpm N_2 flow from the permeation device, were
266   bubbled through the absorption vessel. After a continuous collection for 5 hours, we removed the absorption apparatus
267   from the cooling mixture, and allowed it to warm to room temperature prior to disassembling the setup to prevent any
268   losses of iodine on the tip of the inlet capillary. The absorption vessel was then re-weighed; the mass compared with
269   that prior to absorption was less than 2%, indicating a negligible loss during the trapping process. The I_2 / n-hexane
270   sample solutions were stored at 4 °C for 14 hours before being subjected to analysis.

271

272   We determined the I_2 concentration of the samples using a UV/Vis spectrophotometer (Shimadzu Model UV2450) at
273   a wavelength of 522 nm. We established a calibration curve via a set of I_2 solutions ranging from 270 to 5300 nmol,
274   diluted with n-hexane from a freshly prepared stock solution (0.5 g L^{-1}). Repetition of the same analysis after 2 and 7
275   days yielded identical results, confirming that the sample solutions were stable at 4 °C. As an alternative analytical
276   approach, we also quantified the I_2 concentration in the sample solutions using an inductively coupled plasma mass
277   spectrometer (ICP-MS, Agilent 7800). Before introducing to the ICP-MS, the sample solutions were treated with
278    $NaHSO_3$ water solution (0.100 M), accomplishing efficient hexane-to-water extraction and simultaneous reduction of
279   iodine to iodide (Schwehr et al., 2005) (Agilent Clinical Sample Preparation Guide (v3), *ref.* ISO 17294-2). The ICP-
280   MS results were in good agreement with those from the UV/Vis spectrophotometry.

281

282   We conducted the I_2 trapping and quantification experiments in triplicate with satisfactory reproducibility (standard
283   deviation < 10%). The calculated iodine permeation rate at 50 mlpm N_2 flow and 140 °C oven temperature is $278 \pm$
284   12 ng min^{-1} (mean ± standard deviation). This result was used as the benchmark to estimate temperature-corrected
285   permeation rates according to the formula provided by the permeation tube vendor (VICI Metronic). We checked the
286   validity of the temperature-corrected values by conducting a second iodine absorption experiment in which the iodine
287   permeation tube was kept at 130 °C with an N_2 flow rate of 50 mlpm, and the determined permeation rate agreed
288   within 10% of the calculated value. We then diluted the I_2 flow to seven different values and measured the flow with
289   the Br-MION-CIMS. We repeated the calibration five times; we show the data along with a linear fit between the I_2
290   concentration and normalized I_2 signal in Fig. 4 (a). The slope of the line gives a calibration coefficient of 6.3×10^{10}
291   molec cm^{-3} per normalized signal (cps cps^{-1}), with R^2 of 0.98 and an overall uncertainty of ± 45%.

292
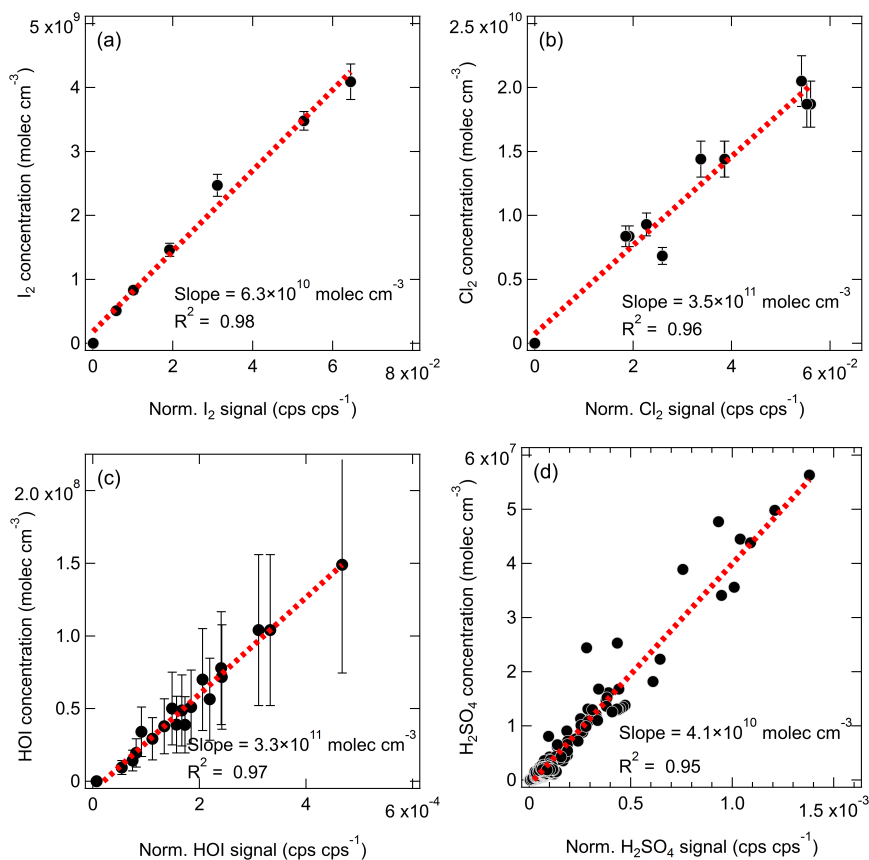
Figure 4. The absolute concentrations (molec cm^{-3}) *vs.* the normalized signals (cps cps^{-1}) measured with the Br-MION-CIMS for (a) I_2, (b) Cl_2, (c) HOI, and (d) H_2SO_4. The red dashed lines are the linear fittings. The overall factor 2 systematic scale uncertainty on $[H_2SO_4]$ is not shown here.

3.3.3 Cl_2 calibration using a permeation tube

We used a commercial chlorine permeation tube (VICI Metronic) as a source for offline calibration. We passed a 20 mlpm high-purity nitrogen (99.999%) flow at room temperature through a 25 cm long stainless-steel tube (½" O.D.) containing the permeation tube. We quantified the permeation rate of Cl_2 following a procedure described in a previous study (Finley and Saltzman, 2008). The output of 20 mlpm flow was bubbled into a buffered aqueous potassium iodide solution (2.0 % KI (*m/v*), prepared in 1.00 mM aqueous phosphate buffer, pH = 7.0) filled in an all-glass two-stage serial absorption apparatus (stage 1 = 100 ml; stage 2 = 50 ml) for 3 hours and kept at room temperature. The Cl_2 oxidized the iodide (I$^-$) into iodine (I_2) once contacting with the KI absorption solution, and the I_2 further reacted with the excess KI present in the absorption solution to form I_3^-, which can be quantified by UV/Vis-spectrophotometry. We analyzed the resulting sample solutions with an UV/Vis spectrophotometer (Shimadzu Model UV-1800) using 1-cm quartz cells at 352 nm, corresponding to the I_3^-. We detected no I_3^- in the second stage absorption solution, indicating that all the chlorine was quantitatively trapped and rapidly converted to I_3^- within the first absorption unit.

310   The samples were quantified relative to I_3^- standards in the range of 5 to 68×10^{-6} M, prepared by dilution of a stock

311   obtained by dissolving 174 mg iodine in 200 ml of a solution containing 2 % KI in 1.00 mM aqueous phosphate buffer,

312   pH 7.0. From this calibration curve, we calculated a molar absorptivity of 26,800 L mol^{-1} cm^{-1}, which is consistent

313   with the values reported in the literature (Finley and Saltzman, 2008; Kazantseva et al., 2002). Samples and standard

314   solutions were re-analyzed after being stored in the dark at room temperature for 24 hours, and the results were within

315   3 % of those obtained with the fresh solutions. We repeated the absorption experiment, and the calculated chlorine

316   permeation rate at room temperature was 764 ± 74 ng Cl_2 min^{-1} (mean ± standard deviation).

317

318   The Cl_2 permeation source was run continuously for 12 hours prior to calibration experiments to ensure complete

319   system equilibrium. A two-stage dilution system similar to the setup of (Gallagher et al., 1997) was set up for diluting

320   the output of the Cl_2 permeation device. The 20 mlpm of N_2 stream emerging from the Cl_2 permeation device (operated

321   at room temperature) was diluted in a stream of 6 slpm of dry N_2. Then, a small fraction of this mixture (50 to 300

322   mlpm) was further mixed with the total flow of 25 slpm of N_2 (20 slpm dry N_2 + 5 slpm humidified N_2) before being

323   sampled by the Br-MION-CIMS. The calibration coefficient for Cl_2 was determined to be 3.5×10^{11} molec cm^{-3} per

324   normalized signal (cps cps^{-1}) from three separate calibration experiments (Fig 4 (b)), with an accuracy of 30 %.

325

326   **3.3.4 HOI calibration using a calibrator**

327   We produced a continuous HOI source via the reaction of I_2 and hydroxyl radical (OH) in a setup similar to the sulfuric

328   acid (H_2SO_4) calibrator (Kürten et al., 2012). The OH was generated by photolyzing H_2O with a mercury (Hg) lamp

329   at 184.9 nm, whose calibrated intensity was used to estimate the OH concentration. We tested the system by removing

330   the I_2 or OH source from the calibrator, upon which HOI production was undetectable, confirming that any single

331   reactant did not produce HOI. A numerical model was constructed to predict the mean HOI concentration entering the

332   Br-MION-CIMS, which is analogous to the model used for H_2SO_4 calibration (Kürten et al., 2012). We only included

333   the formation pathway of I_2 + OH to HOI in the model for simplicity; the other pathway of IO + HO_2 was considered

334   minor as IO forms at a relatively slow rate via the reaction of I radical and O_3. We produced a range of HOI

335   concentrations by varying I_2 and OH concentrations in the calibrator. We show in Fig. 4 (c) the linear correlation

336   between the modeled HOI concentrations and measured HOI signals. The slope of the fit line corresponds to a

337   calibration coefficient of 3.3×10^{11} molec cm^{-3} per normalized signal (cps cps^{-1}), with an overall uncertainty of ± 55%.

338   The good correlation ($R^2 = 0.97$) including various H_2O levels also indicates that H_2O concentrations did not affect

339   the HOI detection.

340

341   **3.3.5 H_2SO_4 calibration using a nitrate-CIMS**

342   We derive the H_2SO_4 calibration coefficient for the Br-MION-CIMS using the absolute H_2SO_4 concentrations

343   measured with a pre-calibrated nitrate-CIMS. The calibration protocol of H_2SO_4 in the nitrate-CIMS has been

344   described in detail previously (Kürten et al., 2012). The H_2SO_4 time series used for the inter-method calibration covers

345   a wide concentration range from less than 5.0×10^4 (detection limit of the nitrate-CIMS) to 6.0×10^7 molec cm^{-3}. For

346   Br-MION-CIMS, although both HSO_4^- and $H_2SO_4 \cdot Br^-$ appear as distinct peaks for sulfuric acid, we only use the

Atmospheric
Measurement
Techniques
Discussions

Open Access

EGU

347   normalized $H_2SO_4\cdot^{79}Br^-$ for the inter-calibration, as HSO_4^- (m/z = 96.96) has substantial interference from the reagent

348   ion $H_2O\cdot^{79}Br^-$ (m/z = 96.93). We show in Fig. 4 (d) the linear fit ($[H_2SO_4] = 4.1\times10^{10}$ molec cm^{-3} × $H_2SO_4\cdot^{79}Br^-/(^{79}Br^-$

349   + $H_2O\cdot^{79}Br^-) - 9.3\times10^5$) between the two H_2SO_4 traces with a correlation coefficient of 0.95. The calculated H_2SO_4

350   calibration coefficient is 4.1×10^{10} molec cm^{-3} per normalized signal (cps cps^{-1}).

351

352   **3.3.6 Connecting sensitivity to binding enthalpy**

353   Beyond the species for which we carried out calibrations, there are many more, especially iodine species, that cannot

354   be directly calibrated due to a lack of authentic standards or generation methods. However, the sensitivity of an iodide-

355   CIMS towards analytes can be predicted by the cluster binding enthalpy, calculated by relatively simple quantum

356   chemical methods (Iyer et al., 2016). This holds for the bromide-CIMS as well. In the instrument, ion clusters, formed

357   from reactions between analytes and reagent ions, are guided and focused by ion optics during transmission to the

358   detector. The electric forces applied to the clusters enhance their collision energies with carrier gas molecules. If

359   sufficient energy is transferred during the collision, cluster fragmentation may occur, affecting the instrument

360   sensitivity for the analytes (Passananti et al., 2019). However, clusters with higher binding enthalpy will be more

361   easily preserved and detected. Analytes that bind to the reagent ions with enthalpies higher than a critical level are

362   likely detected at maximum sensitivity (kinetic-limited detection) by the instrument. For example, the calculated

363   critical enthalpy is 25 kcal mol^{-1} for the iodide-CIMS used in Iyer et al. (Iyer et al., 2016) and Lopez-Hilfiker et al.

364   (Lopez-Hilfiker et al., 2016), calculated at the DLPNO-CCSD(T)/def2-QZVPP//PBE/aug-cc-pVTZ-PP level of theory.

365

366   For the bromide chemical ionization, there are two types of fragmentation pathways:

367   1)   Reversion to the original form of Br$^-$ and analyte

368    $$X\text{-}H\cdot Br^- \rightarrow X\text{-}H + Br^- \qquad\qquad (1)$$

369   2)   Proton transfer from the analyte to Br$^-$

370    $$X\text{-}H\cdot Br^- \rightarrow X^- + HBr \qquad\qquad (2)$$

371   where the X-H is the hydrogen bond donor. An analyte may be expected to be detected at the maximum sensitivity

372   when the dissociation enthalpy for the first pathway is either a) much higher than the critical enthalpy (dissociation

373   back to the reactants does not occur), or b) lower than the critical enthalpy, but much higher than that of the second

374   pathway (dissociation back to the reactants would occur, but it is not competitive with the other dissociation channel).

375   Whether the enthalpy for the second pathway is higher than the critical enthalpy does not directly affect the sensitivity,

376   as both X-H·Br$^-$ and X$^-$ can be measured and counted. Taking H_2SO_4 as an example, the dissociation enthalpies for

377   the first and second pathways are 41.1 and 27.9 kcal mol^{-1}, respectively. If some of the $H_2SO_4\cdot Br^-$ dissociate, they

378   preferably become HSO_4^- and are detectable by the Br-CIMS. We list the cluster formation enthalpies for a selection

379   of halogen containing species in Table 1 and the corresponding cluster dissociation enthalpies in Table 2.

380

381   While we were unable to experimentally establish a correlation between sensitivities and binding enthalpies due to

382   limited quantifiable halogen species, we can predict the tentative critical enthalpy as the binding enthalpy of a species

383   that is likely detected at the maximum sensitivity. Among all the calibration coefficients listed in Table 3, H_2SO_4 and

384   I_2 have the lowest calibration coefficients (highest sensitivities); and their coefficients are almost the same for both

385   the online and offline calibrations, with discrepancies well within the systematic uncertainties. Thereby, we conclude

386   that both H_2SO_4 and I_2 are detected at the maximum sensitivity, suggesting a critical enthalpy not higher than 33.7

387   kcal mol^{-1}. We can then infer the sensitivity for other species that are difficult to calibrate by comparing their binding

388   enthalpies to those of the benchmark species. For example, ICl and IBr should have the maximum sensitivity, since

389   the dissociation enthalpies for $ICl \cdot Br^-$ and $IBr \cdot Br^-$ are both much higher than 33.7 kcal mol^{-1} (Table 2). Although

390    $HIO_3 \cdot Br^-$ has a lower dissociation enthalpy than the critical value, the favored dissociation pathway is proton transfer

391   (the second pathway); HIO_3 can thus be considered as a maximum sensitivity species detectable as IO_3^- ions after

392   proton transfer. This is consistent with the fact that both $HIO_3 \cdot Br^-$ and IO_3^- are detected in Figure 1, so is the case with

393   H_2SO_4. We thus assume that HIO_3 has a kinetic calibration coefficient of 3.8×10^{10} molec cm^{-3} cps cps^{-1}, the value for

394   H_2SO_4. However, the lowest dissociation enthalpies of $HOI \cdot Br^-$ and $Cl_2 \cdot Br^-$ are 26.9 and 22.3 kcal mol^{-1}, respectively,

395   consistent with their higher calibration coefficients of 3.3×10^{11} and 3.5×10^{11} molec cm^{-3} cps cps^{-1}. The dissociation

396   enthalpies for $IO \cdot Br^-$, $OIO \cdot Br^-$, and $HIO_2 \cdot Br^-$ are 24.5, 23.2, and 29.2 kcal mol^{-1}, respectively. We would expect that

397   their sensitives are lower than the maximum sensitivity. Since the dissociation enthalpies for $IO \cdot Br^-$ and $OIO \cdot Br^-$ are

398   between those of $HOI \cdot Br^-$ and $Cl_2 \cdot Br^-$, a similar calibration coefficient of around 3.0×10^{11} molec cm^{-3} cps cps^{-1} could

399   be applied.

400

401   Further, we estimate the detection limit of the calibrated species. The detection limit is defined as the analyte

402   concentration, corresponding to the sum of the mean signal and three times the standard deviations (3σ) of the

403   background fluctuations during a two-hour background measurement. We derive the detection limit of HOI, HIO_3, I_2,

404   and H_2SO_4 to be 5.8×10^6, 1.2×10^5, 6.3×10^5, and 2.0×10^5 molec cm^{-3} (or 0.2, 0.005, 0.03, and 0.008 pptv), respectively,

405   for a 2-min integration time.

406

407   **3.4 Comparison between Br-MION-CIMS and Br-FIGAERO-CIMS**

408   While Br-MION-CIMS and Br-FIGAERO-CIMS use the same chemical ionization scheme, their designs differ in the

409   ion-molecule reaction chamber (IMR). MION is an atmospheric pressure (1 bar) drift tube; analyte molecules gain an

410   electric charge in an axial laminar flow. FIGAERO is connected to a cone-shaped IMR chamber operated at a reduced

411   pressure (150 mbar); the sample flow is injected into the inlet via an orifice, necessarily causing turbulence and wall

412   interactions in the IMR region. The atmospheric pressure and reduced pressure IMRs are both widely used for trace

413   gas measurements. We thus compare iodine species measurements from Br-MION-CIMS and Br-FIGAERO-CIMS,

414   to better understand the performance and applicability of bromide ionization scheme.

415

416   **3.4.1 Signal trend and detection limit**

417   We show in Fig. 5 the same new-particle formation event as in Fig. 2, to illustrate the time series for $HIO_3 \cdot Br^-$, $HOI \cdot Br^-$,

418    $IO \cdot Br^-$, and $I_2 \cdot Br^-$, measured with Br-MION-CIMS (red circles) and Br-FIGAERO-CIMS (grey sticks), respectively.

419   Note that the FIGAERO alternates between gas and particle measurements; here we show only the gas-phase signals.

420   Clear and concurrent signals of HIO_3, HOI, IO, and I_2 are evident from both the Br-MION-CIMS and Br-FIGAERO-

421 CIMS. Prior to the NPF event (08:11), there was no photochemical production and thus virtually no signal of oxidized

422 iodine species in both instruments. The dark reaction of ozone with I_2 did not proceed at a significant rate, due to the

423 low rate coefficient and low levels of I_2. Signals detected during this period are considered as the persistent background,

424 coming from electronic noise or other sources such as the ionizer, carrier flows, or long-term "memory" in the case

425 of the Br-FIGAERO-CIMS. Not surprisingly, the Br-MION-CIMS has a near-zero background for all analytes. For

426 HIO_3 (Fig. 5 (a)), the background signal in the Br-FIGAERO-CIMS is also negligible; however, IO shows a substantial

427 persistent background (Fig. 5 (c)) in the Br-FIGAERO-CIMS. After the NPF event (10:21), the photochemical

428 production of oxidized iodine species was terminated and vapor concentrations decayed exponentially due to dilution

429 and losses to chamber walls. The I_2 signal increases after the event termination because it is no longer photolyzed.

431 Applying the calibration coefficients, we convert the Br-MION-CIMS signals to absolute concentrations, and

432 subsequently correlate them with signals measured with Br-FIGAERO-CIMS. We then estimate the tentative detection

433 limits for HOI and HIO_3 in the Br-FIGAERO-CIMS to be 3.3×10^7 and 5.1×10^6 molec cm^{-3} (versus 5.8×10^6 and 1.2×10^5

434 molec cm^{-3} in the Br-MION-CIMS), respectively, at 3σ of the background signal for a 2-min integration time during

435 a two-hour period; they are in general one order of magnitude higher than those in the Br-MION-CIMS. This is in line

436 with the higher background signals observed in the Br-FIGAERO-CIMS. We are unable to estimate the I_2 detection

437 limit in the Br-FIGAREO-CIMS, due to a lack of I_2 background measurement; but Br-FIGAERO-CIMS can and did

438 detect I_2 at the low pptv level with good fidelity.
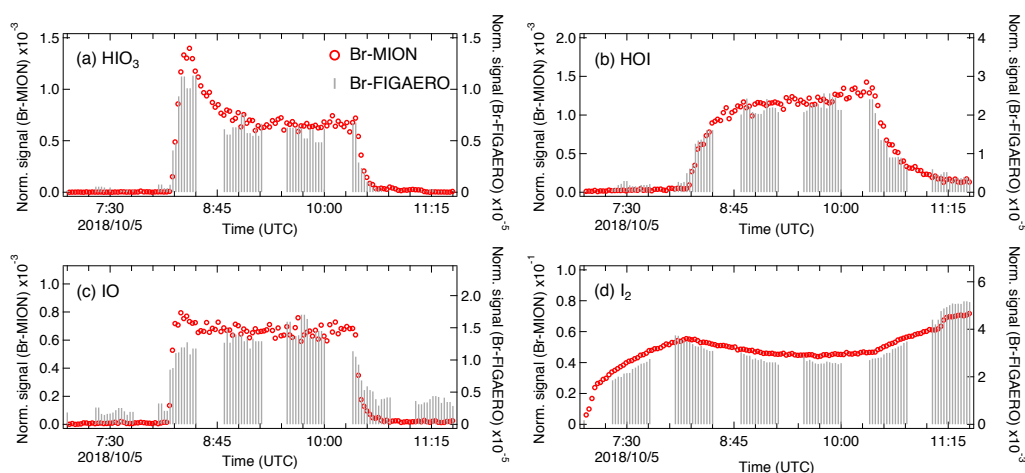
Figure 5. Signal comparison of selected iodine species measured with Br-MION-CIMS and (gas-phase) Br-FIGAERO-CIMS, respectively, during the same iodine new-particle formation experiment shown in Fig. 2.

3.4.2 Rise and decay time constants

445 In order to quantitatively compare the performance of the two types of IMRs, we set the initiation (08:11) and

446 termination (10:21) of NPF event as $t = 0$, and fit the rise and decay rates of HIO_3, HOI and IO in both instruments,

447 respectively.

14

448

449   When we initiated the photochemistry, oxidized iodine species rapidly built up toward an asymptote; we thus fit their

450   time-series signals individually with a four-parameter sigmoid function using a least-squares fitting algorithm:

451    $$S_i(t) = a + (b - a)/\left(1 + e^{(-(t-t_{app})/c)}\right) \qquad (3)$$

452   where a and b represent the background and asymptotic value of the sigmoid function respectively, c is the exponential

453   time constant of the signal change, and t_{app} is the time at which the 50 % value between plateau and background is

454   reached (50 % appearance time). As we were unable to separate the time scale of chemical reactions from that of

455   instrument response, we use the time constants to represent the overall response for the purpose of comparing

456   instrument performance.

457

458   We show in Fig. 6 (a), (c), and (e) the rise rate fits of HIO_3, HOI, and IO, respectively. HIO_3 signals rose with a time

459   constant of 102 s in the Br-MION-CIMS and 108 s in the Br-FIGAERO-CIMS, both with $t_{app}= \sim 300$ s. The fitted time

460   constants of HOI are slightly longer than those of HIO_3, with 120 s in the Br-MION-CIMS and 114 s in the Br-

461   FIGAERO-CIMS. IO signals stabilized the earliest, thus have the fastest time constants of 48 s in the Br-MION-CIMS

462   and 84 s in the Br-FIGAERO-CIMS. The instrumental differences are small for HIO_3 and HOI, but larger for IO. When

463   colliding with the IMR surface, HIO_3 condenses irreversibly; it thus makes sense that the Br-MION-CIMS and Br-

464   FIGAERO-CIMS signals show the same time constant for HIO_3. Semi-volatile HOI, however, can return to the gas

465   phase from the walls depending on the surface coverage of HOI and the vapor concentration. Additionally, the

466   heterogeneous reaction of aqueous iodide (I^-) and ozone (Carpenter et al., 2013) could also contribute to the emission

467   of HOI from the IMR wall in the FIGAERO. As the evaporation flux is typically a function of the amount analyte on

468   the surface, the buffering effect could degrade the instrument time response upon changes in analyte concentration.

469   Here, however, we did not observe a significant memory effect, likely because the HOI concentration was too low to

470   fully saturate the IMR surface or because any HOI evaporation was suppressed due to an enhanced accommodation

471   coefficient of HOI on the metal surface. We expect IO to be prone to loss on the metal surface due to its radical nature.

472

473   We also fit the exponential decay time constants of these iodine species to test this interpretation (Fig. 6 (b), (d), and

474   (f)). After photochemistry was terminated at the end of the NPF event, only two sinks drove the vapor concentration

475   decay – dilution and wall loss. Memory effects could also influence the signal time constant. The dilution loss rate

476   was around 2.1×10^{-4} s^{-1} (4760 s time constant) for all species in the chamber, determined by the total chamber flow

477   rate and the chamber volume. Wall loss rates, however, vary for species with different diffusion constants. The decay

478   rates of HIO_3 are 400 s for the Br-MION-CIMS and 370 s for the Br-FIGAERO-CIMS, much faster than the dilution

479   loss. For comparison, the time constant for H_2SO_4 vapor loss was 300 s. These time constants are thus consistent with

480   wall loss (around 2.2×10^{-3} s^{-1}). The IO decay time constant is 294 s for the Br-MION-CIMS and 435 s for the Br-

481   FIGAERO-CIMS. The time constant for the Br-MION-CIMS indicates that the decay of IO is also driven by wall loss,

482   so the net flux during this period was thus towards the wall rather than from the wall. Therefore, the difference of IO

483   between instruments may well be attributed to the persistent background from the ionizer of the FIGAERO. The HOI

484   signals have longer decay time constants in both instruments of 909 s for the Br-MION-CIMS and 714 s for the Br-

485   FIGAERO-CIMS; this may reflect a time constant for depletion of HOI adsorbed to the chamber walls.

486
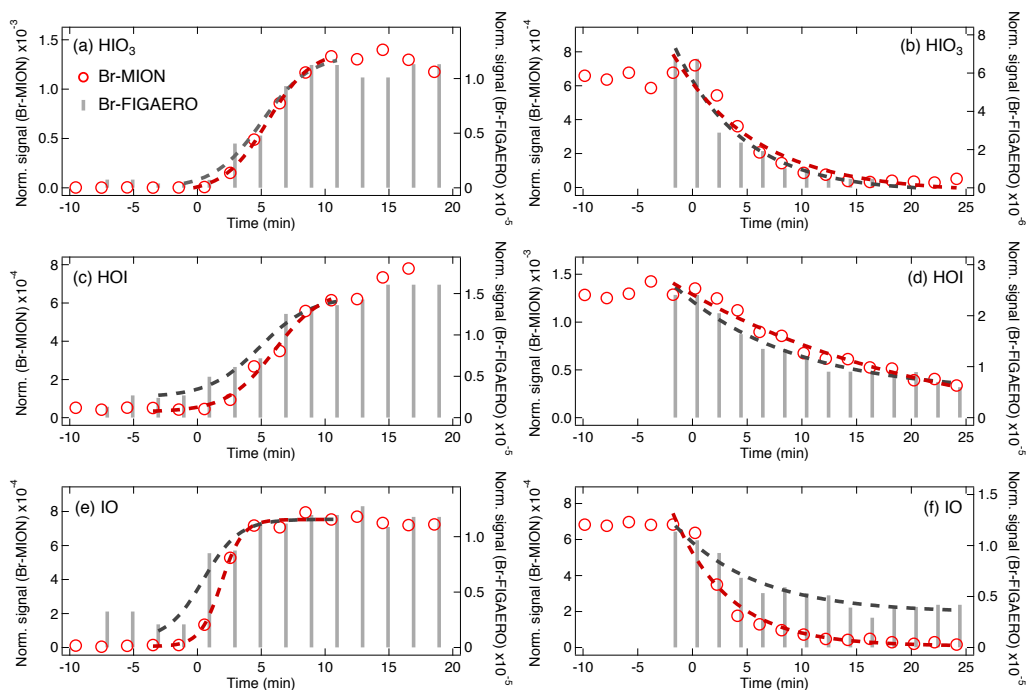
Figure 6. Rising ((a), (c), and (e)) and decay ((b), (d), and (f)) rate comparison of selected iodine species measured with Br-MION-CIMS and Br-FIGAERO-CIMS, respectively, during the same iodine new-particle formation event in Fig. 2 and 5.

4 Summary and conclusion

492   We confirm in this study that bromide chemical ionization is a suitable technique for the time-resolved, highly

493   sensitive, and simultaneous measurements of iodine species and sulfuric acid. The Br-MION-CIMS shows constant

494   sensitivity throughout the relative humidity range of 40 to 80 % at -10 °C, as long as the sum of the two reagent ions

495   (Br^- + $H_2O \cdot Br^-$) is used for signal normalization. This demonstrates the applicability of this technique to field

496   measurements in the ambient marine environment.

497

498   We quantify iodine species and sulfuric acid via offline calibrations (i.e. permeation tube and calibrator) and inter-

499   method calibrations (i.e. CE-DOAS and pre-calibrated nitrate-CIMS); different methods result in consistent

500   calibration coefficients. Further, we calculate the binding enthalpies between the calibrated species and reagent ions,

501   which qualitatively agree with the corresponding calibration coefficients. This indicates that the quantum chemical

502   calculations can be employed along with the calibration experiments to determine the sensitivities for unquantifiable

503   species; more work is required to further establish the correlation between calibration coefficients and binding

504   enthalpies.

505

506 Further, using inter-method and offline calibrations, we estimate the detection limits of HOI, HIO_3, I_2, and H_2SO_4 in

507 Br-MION-CIMS being 5.8×10^6, 1.2×10^5, 6.3×10^5, and 2.0×10^5 molec cm^{-3}, respectively, for a 2-min integration time

508 during a two-hour period. To our knowledge, the simultaneous measurements of various iodine species and sulfuric

509 acid with low detection limits are unprecedented for online techniques. Detection limits for HOI and HIO_3 in the Br-

510 FIGAERO-CIMS are 3.3×10^7 and 5.1×10^6 molec cm^{-3}, which are in general one order of magnitude higher than those

511 in the Br-MION-CIMS. The signal comparison between the two instruments also shows that the Br-CIMS can be

512 coupled to both the atmospheric pressure and the reduced pressure interfaces for iodine species and sulfuric acid

513 measurements in the marine environment.

514

515

516 *Data availability.* Data available on request from the authors.

517

518 *Author Contributions.* M.W., X.-C.H., Y.-J.T and H.F. wrote the manuscript. X.-C.H., Y.-J.T., M.W. and M.Sip.

519 designed the experiments. X.-C.H., Y.-J.T. and J.S. carried out the Br-MION-CIMS measurements, M.W., D.C. and

520 V.H. carried out the Br-FIGAERO-CIMS measurements, and H.F. carried out the CE-DOAS measurements. Y.-J.T.,

521 X.-C.H., H.F., D.C., J.S. and M.Sim. performed the calibrations. S.I., X.-C.H. and T.K. carried out the quantum

522 chemical calculations. M.W. performed the comparison analysis of the Br-FIGAERO-CIMS and Br-MION-CIMS.

523 N.-M.D., T.K., M.R., R.V and M.Sip. commented on the manuscript. All other co-authors participated in either the

524 development and preparations of the CLOUD facility and the instruments, and/or collecting and analyzing the data.

525

526 *Competing interests.* The authors declare that they have no conflict of interest.

527

537

538 **References**

539 Bitter, M., Ball, S. M., Povey, I. M. and Jones, R. L.: A broadband cavity ringdown spectrometer for in-situ

540 measurements of atmospheric trace gases, Atmos. Chem. Phys., doi:10.5194/acp-5-2547-2005, 2005.

541 Carpenter, L. J., MacDonald, S. M., Shaw, M. D., Kumar, R., Saunders, R. W., Parthipan, R., Wilson, J. and Plane,

542 J. M. C.: Atmospheric iodine levels influenced by sea surface emissions of inorganic iodine, Nat. Geosci.,

543 doi:10.1038/ngeo1687, 2013.

544 Chai, J. Da and Head-Gordon, M.: Long-range corrected hybrid density functionals with damped atom-atom

545 dispersion corrections, Phys. Chem. Chem. Phys., doi:10.1039/b810189b, 2008.

546 Chance, R. J., Shaw, M., Telgmann, L., Baxter, M. and Carpenter, L. J.: A comparison of spectrophotometric and

547 denuder based approaches for the determination of gaseous molecular iodine, Atmos. Meas. Tech., doi:10.5194/amt-

548 3-177-2010, 2010.

549 Dias, A., Ehrhart, S., Vogel, A., Mathot, S., Onnela, A., Almeida, J., Kirkby, J., Williamson, C. and Mumford, S.:

Atmospheric
Measurement
Techniques
Discussions

EGU

550   Temperature uniformity in the CERN CLOUD chamber, Atmos. Meas. Tech., 10, 5075–5088, 2017.

551   Dillon, T. J., Tucceri, M. E. and Crowley, J. N.: Laser induced fluorescence studies of iodine oxide chemistry: Part
552   II. The reactions of IO with CH3O2, CF3O2 and O3, Phys. Chem. Chem. Phys., doi:10.1039/b611116e, 2006.

553   Duplissy, J., Merikanto, J., Franchin, A., Tsagkogeorgas, G., Kangasluoma, J., Wimmer, D., Vuollekoski, H.,
554   Schobesberger, S., Lehtipalo, K., Flagan, R. C., Brus, D., Donahue, N. M., Vehkamaki, H., Almeida, J., Amorim,
555   A., Barmet, P., Bianchi, F., Breitenlechner, M., Dunne, E. M., Guida, R., Henschel, H., Junninen, H., Kirkby, J.,
556   Kurten, A., Kupc, A., Maattanen, A., Makhmutov, V., Mathot, S., Nieminen, T., Onnela, A., Praplan, A. P.,
557   Riccobono, F., Rondo, L., Steiner, G., Tome, A., Walther, H., Baltensperger, U., Carslaw, K. S., Dommen, J.,
558   Hansel, A., Petaja, T., Sipila, M., Stratmann, F., Vrtala, A., Wagner, P. E., Worsnop, D. R., Curtius, J. and Kulmala,
559   M.: Effect of ions on sulfuric acid-water binary particle formation: 2. Experimental data and comparison with QC-
560   normalized classical nucleation theory, J. Geophys. Res., 121, 1752–1775, doi:10.1002/2015JD023539, 2016.

561   Feller, D.: The role of databases in support of computational chemistry calculations, J. Comput. Chem.,
562   doi:10.1002/(SICI)1096-987X(199610)17:13<1571::AID-JCC9>3.0.CO;2-P, 1996.

563   Finley, B. D. and Saltzman, E. S.: Observations of Cl2, Br2, and I2 in coastal marine air, J. Geophys. Res. Atmos.,
564   doi:10.1029/2008JD010269, 2008.

565   Frisch, M. J., Trucks, G. W., Schlegel, H. B., Scuseria, G. E., Robb, M. A., Cheeseman, J. R., Scalmani, G., Barone,
566   V., Mennucci, B., Petersson, G. A., Nakatsuji, H., Caricato, M., Li, X., Hratchian, H. P., Izmaylov, A. F., Bloino, J.,
567   Zheng, G., Sonnenberg, J. L., Hada, M., Ehara, M., Toyota, K., Fukuda, R., Hasegawa, J., Ishida, M., Nakajima, T.,
568   Honda, Y., Kitao, O., Nakai, H., Vreven, T., Montgomery Jr., J. A., Peralta, J. E., Ogliaro, F., Bearpark, M., Heyd, J.
569   J., Brothers, E., Kudin, K. N., Staroverov, V. N., Kobayashi, R., Normand, J., Raghavachari, K., Rendell, A.,
570   Burant, J. C., Iyengar, S. S., Tomasi, J., Cossi, M., Rega, N., Millam, J. M., Klene, M., Knox, J. E., Cross, J. B.,
571   Bakken, V., Adamo, C., Jaramillo, J., Gomperts, R., Stratmann, R. E., Yazyev, O., Austin, A. J., Cammi, R.,
572   Pomelli, C., Ochterski, J. W., Martin, R. L., Morokuma, K., Zakrzewski, V. G., Voth, G. A., Salvador, P.,
573   Dannenberg, J. J., Dapprich, S., Daniels, A. D., Farkas, ., Foresman, J. B., Ortiz, J. V, Cioslowski, J. and Fox, D.
574   J.: Gaussian09 Revision D.01, Gaussian Inc. Wallingford CT, Gaussian 09 Revis. C.01, 2010.

575   Gallagher, M. S., King, D. B., Whung, P. Y. and Saltzman, E. S.: Performance of the HPLC/fluorescence SO2
576   detector during the GASIE instrument intercomparison experiment, J. Geophys. Res. Atmos.,
577   doi:10.1029/97jd00700, 1997.

578   Gómez Martín, J. C., Blahins, J., Gross, U., Ingham, T., Goddard, A., Mahajan, A. S., Ubelis, A. and Saiz-Lopez,
579   A.: In situ detection of atomic and molecular iodine using Resonance and Off-Resonance Fluorescence by Lamp
580   Excitation: ROFLEX, Atmos. Meas. Tech., doi:10.5194/amt-4-29-2011, 2011.

581   Gómez Martín, J. C., Gálvez, O., Baeza-Romero, M. T., Ingham, T., Plane, J. M. C. and Blitz, M. A.: On the
582   mechanism of iodine oxide particle formation, Phys. Chem. Chem. Phys., doi:10.1039/c3cp51217g, 2013.

583   He, X.-C., Iyer, S., Sipilä, M., Ylisirniö, A., Peltola, M., Kontkanen, J., Baalbaki, R., Simon, M., Kürten, A., Tham,
584   Y. J. and others: Determination of the Collision Rate Coefficient between Charged Iodic Acid Clusters and Iodic
585   Acid using the Appearance Time Method, Aerosol Sci. Technol., 1–17, 2020.

586   Iyer, S., Lopez-Hilfiker, F., Lee, B. H., Thornton, J. A. and Kurtén, T.: Modeling the Detection of Organic and
587   Inorganic Compounds Using Iodide-Based Chemical Ionization, J. Phys. Chem. A, doi:10.1021/acs.jpca.5b09837,
588   2016.

589   Junninen, H., Ehn, M., Petaja, T., Luosujarvi, L., Kotiaho, T., Kostiainen, R., Rohner, U., Gonin, M., Fuhrer, K.,
590   Kulmala, M., Worsnop, D. R., Petäjä, T., Luosujärvi, L., Kotiaho, T., Kostiainen, R., Rohner, U., Gonin, M., Fuhrer,
591   K., Kulmala, M. and Worsnop, D. R.: A high-resolution mass spectrometer to measure atmospheric ion composition,
592   Atmos. Meas. Tech., 3(4), 1039–1053, doi:10.5194/amt-3-1039-2010, 2010.

593   Kazantseva, N. N., Ernepesova, A., Khodjamamedov, A., Geldyev, O. A. and Krumgalz, B. S.: Spectrophotometric
594   analysis of iodide oxidation by chlorine in highly mineralized solutions, in Analytica Chimica Acta., 2002.

595   Kendall, R. A., Dunning, T. H. and Harrison, R. J.: Electron affinities of the first-row atoms revisited. Systematic
596   basis sets and wave functions, J. Chem. Phys., doi:10.1063/1.462569, 1992.

597   Kercher, J. P., Riedel, T. P. and Thornton, J. A.: Chlorine activation by N2O5: Simultaneous, in situ detection of
598   ClNO2 and N2O5 by chemical ionization mass spectrometry, Atmos. Meas. Tech., doi:10.5194/amt-2-193-2009,

599   2009.

600   Kirkby, J., Curtius, J., Almeida, J., Dunne, E., Duplissy, J., Ehrhart, S., Franchin, A., Gagné, S., Ickes, L., Kürten,
601   A., Kupc, A., Metzger, A., Riccobono, F., Rondo, L., Schobesberger, S., Tsagkogeorgas, G., Wimmer, D., Amorim,
602   A., Bianchi, F., Breitenlechner, M., David, A., Dommen, J., Downard, A., Ehn, M., Flagan, R. C., Haider, S.,
603   Hansel, A., Hauser, D., Jud, W., Junninen, H., Kreissl, F., Kvashin, A., Laaksonen, A., Lehtipalo, K., Lima, J.,
604   Lovejoy, E. R., Makhmutov, V., Mathot, S., Mikkilä, J., Minginette, P., Mogo, S., Nieminen, T., Onnela, A.,
605   Pereira, P., Petäjä, T., Schnitzhofer, R., Seinfeld, J. H., Sipilä, M., Stozhkov, Y., Stratmann, F., Tomé, A.,
606   Vanhanen, J., Viisanen, Y., Vrtala, A., Wagner, P. E., Walther, H., Weingartner, E., Wex, H., Winkler, P. M.,
607   Carslaw, K. S., Worsnop, D. R., Baltensperger, U. and Kulmala, M.: Role of sulphuric acid, ammonia and galactic
608   cosmic rays in atmospheric aerosol nucleation, Nature, 476, 429 [online] Available from:
609   https://doi.org/10.1038/nature10343, 2011.

610   Kirkby, J., Duplissy, J., Sengupta, K., Frege, C., Gordon, H., Williamson, C., Heinritzi, M., Simon, M., Yan, C.,
611   Almeida, J., Trostl, J., Nieminen, T., Ortega, I. K., Wagner, R., Adamov, A., Amorim, A., Bernhammer, A. K.,
612   Bianchi, F., Breitenlechner, M., Brilke, S., Chen, X. M., Craven, J., Dias, A., Ehrhart, S., Flagan, R. C., Franchin,
613   A., Fuchs, C., Guida, R., Hakala, J., Hoyle, C. R., Jokinen, T., Junninen, H., Kangasluoma, J., Kim, J., Krapf, M.,
614   Kurten, A., Laaksonen, A., Lehtipalo, K., Makhmutov, V., Mathot, S., Molteni, U., Onnela, A., Perakyla, O., Piel,
615   F., Petaja, T., Praplan, A. P., Pringle, K., Rap, A., Richards, N. A. D. D., Riipinen, I., Rissanen, M. P., Rondo, L.,
616   Sarnela, N., Schobesberger, S., Scott, C. E., Seinfeld, J. H., Sipila, M., Steiner, G., Stozhkov, Y., Stratmann, F.,
617   Tome, A., Virtanen, A., Vogel, A. L., Wagner, A. C., Wagner, P. E., Weingartner, E., Wimmer, D., Winkler, P. M.,
618   Ye, P., Zhang, X., Hansel, A., Dommen, J., Donahue, N. M., Worsnop, D. R., Baltensperger, U., Kulmala, M.,
619   Carslaw, K. S., Curtius, J., Tomé, A., Virtanen, A., Vogel, A. L., Wagner, A. C., Wagner, P. E., Weingartner, E.,
620   Wimmer, D., Winkler, P. M., Ye, P. L., Zhang, X., Hansel, A., Dommen, J., Donahue, N. M., Worsnop, D. R.,
621   Baltensperger, U., Kulmala, M., Carslaw, K. S. and Curtius, J.: Ion-induced nucleation of pure biogenic particles,
622   Nature, 533(7604), 521–526, doi:10.1038/nature17953, 2016.

623   Koenig, T. K., Baidar, S., Campuzano-Jost, P., Cuevas, C. A., Dix, B., Fernandez, R. P., Guo, H., Hall, S. R.,
624   Kinnison, D., Nault, B. A., Ullmann, K., Jimenez, J. L., Saiz-Lopez, A. and Volkamer, R.: Quantitative detection of
625   iodine in the stratosphere, Proc. Natl. Acad. Sci. U. S. A., doi:10.1073/pnas.1916828117, 2020.

626   Kurten, A., Rondo, L., Ehrhart, S. and Curtius, J.: Calibration of a Chemical Ionization Mass Spectrometer for the
627   Measurement of Gaseous Sulfuric Acid, J. Phys. Chem. A, 116, 6375–6386, doi:Doi 10.1021/Jp212123n, 2012.

628   Lawler, M. J., Sander, R., Carpenter, L. J., Lee, J. D., Von Glasow, R., Sommariva, R. and Saltzman, E. S.: HOCl
629   and Cl2 observations in marine air, Atmos. Chem. Phys., doi:10.5194/acp-11-7617-2011, 2011.

630   Lee, B. H., Lopez-Hilfiker, F. D., Mohr, C., Kurten, T., Worsnop, D. R. and Thornton, J. A.: An iodide-adduct high-
631   resolution time-of-flight chemical-ionization mass spectrometer: application to atmospheric inorganic and organic
632   compounds, Env. Sci Technol, 48(11), 6309–6317, doi:10.1021/es500362a, 2014.

633   Lee, B. H., Lopez-Hilfiker, F. D., Veres, P. R., McDuffie, E. E., Fibiger, D. L., Sparks, T. L., Ebben, C. J., Green, J.
634   R., Schroder, J. C., Campuzano-Jost, P., Iyer, S., D'Ambro, E. L., Schobesberger, S., Brown, S. S., Wooldridge, P.
635   J., Cohen, R. C., Fiddler, M. N., Bililign, S., Jimenez, J. L., Kurtén, T., Weinheimer, A. J., Jaegle, L. and Thornton,
636   J. A.: Flight Deployment of a High-Resolution Time-of-Flight Chemical Ionization Mass Spectrometer:
637   Observations of Reactive Halogen and Nitrogen Oxide Species, J. Geophys. Res. Atmos.,
638   doi:10.1029/2017JD028082, 2018.

639   Leigh, R. J., Ball, S. M., Whitehead, J., Leblanc, C., Shillings, A. J. L., Mahajan, A. S., Oetjen, H., Lee, J. D., Jones,
640   C. E., Dorsey, J. R., Gallagher, M., Jones, R. L., Plane, J. M. C., Potin, P. and McFiggans, G.: Measurements and
641   modelling of molecular iodine emissions, transport and photodestruction in the coastal region around Roscoff,
642   Atmos. Chem. Phys., doi:10.5194/acp-10-11823-2010, 2010.

643   Lopez-Hilfiker, F. D., Mohr, C., Ehn, M., Rubach, F., Kleist, E., Wildt, J., Mentel, T. F., Lutz, A., Hallquist, M.,
644   Worsnop, D. and Thornton, J. A.: A novel method for online analysis of gas and particle composition: description
645   and evaluation of a Filter Inlet for Gases and AEROsols (FIGAERO), Atmos. Meas. Tech., 7(4), 983–1001,
646   doi:10.5194/amt-7-983-2014, 2014.

647   Lopez-Hilfiker, F. D., Iyer, S., Mohr, C., Lee, B. H., D'ambro, E. L., Kurtén, T. and Thornton, J. A.: Constraining
648   the sensitivity of iodide adduct chemical ionization mass spectrometry to multifunctional organic molecules using
649   the collision limit and thermodynamic stability of iodide ion adducts, Atmos. Meas. Tech., doi:10.5194/amt-9-1505-

Atmospheric
Measurement
Techniques
Discussions

Open Access

EGU

650   2016, 2016.

651   Marcy, T. P., Fahey, D. W., Gao, R. S., Popp, P. J., Richard, E. C., Thompson, T. L., Rosenlof, K. H., Ray, E. A.,
652   Salawitch, R. J., Atherton, C. S., Bergmann, D. J., Ridley, B. A., Weinheimer, A. J., Loewenstein, M., Weinstock, E.
653   M. and Mahoney, M. J.: Quantifying Stratospheric Ozone in the Upper Troposphere with in Situ Measurements of
654   HCl, Science (80-.)., doi:10.1126/science.1093418, 2004.

655   McFiggans, G., Coe, H., Burgess, R., Allan, J., Cubison, M., Alfarra, M. R., Saunders, R., Saiz-Lopez, A., Plane, J.
656   M. C., Wevill, D. J., Carpenter, L. J., Rickard, A. R. and Monks, P. S.: Direct evidence for coastal iodine particles
657   from Laminaria macroalgae - Linkage to emissions of molecular iodine, Atmos. Chem. Phys., doi:10.5194/acp-4-
658   701-2004, 2004.

659   Meinen, J., Thieser, J., Platt, U. and Leisner, T.: Technical Note: Using a high finesse optical resonator to provide a
660   long light path for differential optical absorption spectroscopy: CE-DOAS, Atmos. Chem. Phys., doi:10.5194/acp-
661   10-3901-2010, 2010.

662   Neese, F.: The ORCA program system, Wiley Interdiscip. Rev. Comput. Mol. Sci., doi:10.1002/wcms.81, 2012.

663   O'dowd, C. D., Jimenez, J. L., Bahreini, R., Flagan, R. C., Seinfeld, J. H., Hämerl, K., Pirjola, L., Kulmala, M. and
664   Hoffmann, T.: Marine aerosol formation from biogenic iodine emissions, Nature, doi:10.1038/nature00775, 2002.

665   Passananti, M., Zapadinsky, E., Zanca, T., Kangasluoma, J., Myllys, N., Rissanen, M. P., Kurtén, T., Ehn, M.,
666   Attoui, M. and Vehkamäki, H.: How well can we predict cluster fragmentation inside a mass spectrometer?, Chem.
667   Commun., doi:10.1039/c9cc02896j, 2019.

668   Pfeifer, J., Simon, M., Heinritzi, M., Piel, F., Weitz, L., Wang, D., Granzin, M., Müller, T., Bräkling, S., Kirkby, J.,
669   Curtius, J. and Kürten, A.: Measurement of ammonia, amines and iodine compounds using protonated water cluster
670   chemical ionization mass spectrometry, Atmos. Meas. Tech., doi:10.5194/amt-13-2501-2020, 2020.

671   Prados-Roman, C., Cuevas, C. A., Fernandez, R. P., Kinnison, D. E., Lamarque, J. F. and Saiz-Lopez, A.: A
672   negative feedback between anthropogenic ozone pollution and enhanced ocean emissions of iodine, Atmos. Chem.
673   Phys., doi:10.5194/acp-15-2215-2015, 2015.

674   Raso, A. R. W., Custard, K. D., May, N. W., Tanner, D., Newburn, M. K., Walker, L., Moore, R. J., Huey, L. G.,
675   Alexander, L., Shepson, P. B. and Pratt, K. A.: Active molecular iodine photochemistry in the Arctic, Proc. Natl.
676   Acad. Sci. U. S. A., doi:10.1073/pnas.1702803114, 2017.

677   Riplinger, C. and Neese, F.: An efficient and near linear scaling pair natural orbital based local coupled cluster
678   method, J. Chem. Phys., doi:10.1063/1.4773581, 2013.

679   Rissanen, M. P., Mikkilä, J., Iyer, S. and Hakala, J.: Multi-scheme chemical ionization inlet (MION) for fast
680   switching of reagent ion chemistry in atmospheric pressure chemical ionization mass spectrometry (CIMS)
681   applications, Atmos. Meas. Tech., doi:10.5194/amt-12-6635-2019, 2019.

682   Rothman, L. S., Gordon, I. E., Barber, R. J., Dothe, H., Gamache, R. R., Goldman, A., Perevalov, V. I., Tashkun, S.
683   A. and Tennyson, J.: HITEMP, the high-temperature molecular spectroscopic database, J. Quant. Spectrosc. Radiat.
684   Transf., doi:10.1016/j.jqsrt.2010.05.001, 2010.

685   Saiz-Lopez, A., Plane, J. M. C., Baker, A. R., Carpenter, L. J., Von Glasow, R., Gómez Martín, J. C., McFiggans, G.
686   and Saunders, R. W.: Atmospheric chemistry of iodine, Chem. Rev., doi:10.1021/cr200029u, 2012.

687   Sanchez, J., Tanner, D. J., Chen, D., Huey, L. G. and Ng, N. L.: A new technique for the direct detection of HO2
688   radicals using bromide chemical ionization mass spectrometry (Br-CIMS): Initial characterization, Atmos. Meas.
689   Tech., doi:10.5194/amt-9-3851-2016, 2016.

690   Schnitzhofer, R., Metzger, A., Breitenlechner, M., Jud, W., Heinritzi, M., De Menezes, L.-P., Duplissy, J., Guida,
691   R., Haider, S., Kirkby, J. and others: Characterisation of organic contaminants in the CLOUD chamber at CERN,
692   Atmos. Meas. Tech., 7(7), 2159–2168, 2014.

693   Schwehr, K. A., Santschi, P. H. and Elmore, D.: The dissolved organic iodine species of the isotopic ratio of
694   129I/127I: A novel tool for tracing terrestrial organic carbon in the estuarine surface waters of Galveston Bay,
695   Texas, Limnol. Oceanogr. Methods, doi:10.4319/lom.2005.3.326, 2005.

696   Sherwen, T., Evans, M. J., Carpenter, L. J., Andrews, S. J., Lidster, R. T., Dix, B., Koenig, T. K., Sinreich, R.,

Atmospheric
Measurement
Techniques
Discussions

697   Ortega, I., Volkamer, R., Saiz-Lopez, A., Prados-Roman, C., Mahajan, A. S. and Ordóñez, C.: Iodine's impact on
698   tropospheric oxidants: A global model study in GEOS-Chem, Atmos. Chem. Phys., doi:10.5194/acp-16-1161-2016,
699   2016.

700   Simpson, W. R., Brown, S. S., Saiz-Lopez, A., Thornton, J. A. and Von Glasow, R.: Tropospheric Halogen
701   Chemistry: Sources, Cycling, and Impacts, Chem. Rev., doi:10.1021/cr5006638, 2015.

702   Sipilä, M., Sarnela, N., Jokinen, T., Henschel, H., Junninen, H., Kontkanen, J., Richters, S., Kangasluoma, J.,
703   Franchin, A., Peräkylä, O., Rissanen, M. P., Ehn, M., Vehkamäki, H., Kurten, T., Berndt, T., Petäjä, T., Worsnop,
704   D., Ceburnis, D., Kerminen, V. M., Kulmala, M. and O'Dowd, C.: Molecular-scale evidence of aerosol particle
705   formation via sequential addition of HIO3, Nature, doi:10.1038/nature19314, 2016.

706   Spietz, P., Martín, J. G. and Burrows, J. P.: Effects of column density on i2 spectroscopy and a determination of i2
707   absorption cross section at 500 nm, Atmos. Chem. Phys., doi:10.5194/acp-6-2177-2006, 2006.

708   Spolaor, A., Gabrieli, J., Martma, T., Kohler, J., Björkman, M. B., Isaksson, E., Varin, C., Vallelonga, P., Plane, J.
709   M. C. and Barbante, C.: Sea ice dynamics influence halogen deposition to Svalbard, Cryosphere, doi:10.5194/tc-7-
710   1645-2013, 2013.

711   Thalman, R. and Volkamer, R.: Temperature dependent absorption cross-sections of O2-O 2 collision pairs between
712   340 and 630 nm and at atmospherically relevant pressure, Phys. Chem. Chem. Phys., doi:10.1039/c3cp50968k,
713   2013.

714   Tham, Y. J., Wang, Z., Li, Q., Yun, H., Wang, W., Wang, X., Xue, L., Lu, K., Ma, N., Bohn, B., Li, X., Kecorius,
715   S., Größ, J., Shao, M., Wiedensohler, A., Zhang, Y. and Wang, T.: Significant concentrations of nitryl chloride
716   sustained in the morning: Investigations of the causes and impacts on ozone production in a polluted region of
717   northern China, Atmos. Chem. Phys., doi:10.5194/acp-16-14959-2016, 2016.

718   Vandaele, A. C., Hermans, C., Simon, P. C., Carleer, M., Colin, R., Fally, S., Mérienne, M. F., Jenouvrier, A. and
719   Coquart, B.: Measurements of the NO2 absorption cross-section from 42 000 cm-1 to 10 000 cm-1 (238-1000 nm) at
720   220 K and 294 K, J. Quant. Spectrosc. Radiat. Transf., doi:10.1016/S0022-4073(97)00168-4, 1998.

721   Vaughan, S., Gherman, T., Ruth, A. A. and Orphal, J.: Incoherent broad-band cavity-enhanced absorption
722   spectroscopy of the marine boundary layer species I2, IO and OIO, Phys. Chem. Chem. Phys.,
723   doi:10.1039/b802618a, 2008.

724   Wang, M., Kong, W., Marten, R., He, X. C., Chen, D., Pfeifer, J., Heitto, A., Kontkanen, J., Dada, L., Kürten, A.,
725   Yli-Juuti, T., Manninen, H. E., Amanatidis, S., Amorim, A., Baalbaki, R., Baccarini, A., Bell, D. M., Bertozzi, B.,
726   Bräkling, S., Brilke, S., Murillo, L. C., Chiu, R., Chu, B., De Menezes, L. P., Duplissy, J., Finkenzeller, H.,
727   Carracedo, L. G., Granzin, M., Guida, R., Hansel, A., Hofbauer, V., Krechmer, J., Lehtipalo, K., Lamkaddam, H.,
728   Lampimäki, M., Lee, C. P., Makhmutov, V., Marie, G., Mathot, S., Mauldin, R. L., Mentler, B., Müller, T., Onnela,
729   A., Partoll, E., Petäjä, T., Philippov, M., Pospisilova, V., Ranjithkumar, A., Rissanen, M., Rörup, B., Scholz, W.,
730   Shen, J., Simon, M., Sipilä, M., Steiner, G., Stolzenburg, D., Tham, Y. J., Tomé, A., Wagner, A. C., Wang, D. S.,
731   Wang, Y., Weber, S. K., Winkler, P. M., Wlasits, P. J., Wu, Y., Xiao, M., Ye, Q., Zauner-Wieczorek, M., Zhou, X.,
732   Volkamer, R., Riipinen, I., Dommen, J., Curtius, J., Baltensperger, U., Kulmala, M., Worsnop, D. R., Kirkby, J.,
733   Seinfeld, J. H., El-Haddad, I., Flagan, R. C. and Donahue, N. M.: Rapid growth of new atmospheric particles by
734   nitric acid and ammonia condensation, Nature, doi:10.1038/s41586-020-2270-4, 2020.

735   Washenfelder, R. A., Langford, A. O., Fuchs, H. and Brown, S. S.: Measurement of glyoxal using an incoherent
736   broadband cavity enhanced absorption spectrometer, Atmos. Chem. Phys., doi:10.5194/acp-8-7779-2008, 2008.

737

738

739 **Table 1: Cluster formation enthalpies of different species with bromide ion.** The cluster geometries are optimized

740 at the ωB97X-D/aug-cc-pVTZ-PP level at 298.15 K. The enthalpies are calculated at the DLPNO-CCSD(T)/def2-

741 QZVPP//ωB97xD/aug-cc-pVTZ-PP level at 298.15 K.

Cluster formation pathway	Formation enthalpies (kcal mol^{-1})
$Cl_2 + Br^- \rightarrow Cl_2 \cdot Br^-$	-22.3
$OIO + Br^- \rightarrow OIO \cdot Br^-$	-23.2
$IO + Br^- \rightarrow IO \cdot Br^-$	-24.5
$HIO_3 + Br^- \rightarrow HIO_3 \cdot Br^-$	-26.6
$HOI + Br^- \rightarrow HOI \cdot Br^-$	-26.9
$HIO_2 + Br^- \rightarrow HIO_2 \cdot Br^-$	-29.2
$I_2 + Br^- \rightarrow I_2 \cdot Br^-$	-33.7
$ICl + Br^- \rightarrow ICl \cdot Br^-$	-33.8
$IBr + Br^- \rightarrow IBr \cdot Br^-$	-36.7
$H_2SO_4 + Br^- \rightarrow H_2SO_4 \cdot Br^-$	-41.1
$I_2O_4 + Br^- \rightarrow I_2O_4 \cdot Br^-$	-42.6
$I_2O_5 + Br^- \rightarrow I_2O_5 \cdot Br^-$	-53.2

742

743 **Table 2: Fragmentation reaction enthalpies of different species with bromide ion.** The cluster geometries are

744 optimized at the ωB97X-D/aug-cc-pVTZ-PP level at 298.15 K. The enthalpies are calculated at the DLPNO-

745 CCSD(T)/def2-QZVPP//ωB97xD/aug-cc-pVTZ-PP level at 298.15 K.

Cluster fragmentation pathway	Fragmentation enthalpies (kcal mol^{-1})
$Cl_2 \cdot Br^- \rightarrow Cl_2 + Br^-$	22.3
$Cl_2 \cdot Br^- \rightarrow BrCl + Cl^-$	22.3
$HIO_3 \cdot Br^- \rightarrow HIO_3 + Br^-$	26.6
$HIO_3 \cdot Br^- \rightarrow IO_3^- + HBr$	20.8
$HIO_3 \cdot Br^- \rightarrow IO_2^- + HOBr$	52.0
$HOI \cdot Br^- \rightarrow HOI + Br^-$	26.9
$HOI \cdot Br^- \rightarrow IO^- + HBr$	57.7
$HOI \cdot Br^- \rightarrow I^- + HOBr$	31.3
$HIO_2 \cdot Br^- \rightarrow HIO_2 + Br^-$	29.2
$HIO_2 \cdot Br^- \rightarrow IO_2^- + HBr$	43.8
$HIO_2 \cdot Br^- \rightarrow IO^- + HOBr$	42.2
$I_2 \cdot Br^- \rightarrow I_2 + Br^-$	33.7

Atmospheric
Measurement
Techniques
Discussions

$I_2 \cdot Br^- \rightarrow IBr + I^-$	33.8
$ICl \cdot Br^- \rightarrow ICl + Br^-$	33.8
$ICl \cdot Br^- \rightarrow IBr + Cl^-$	39.8
$ICl \cdot Br^- \rightarrow BrCl + I^-$	42.0
$IBr \cdot Br^- \rightarrow IBr + Br^-$	36.7
$IBr \cdot Br^- \rightarrow Br_2 + I^-$	39.4
$H_2SO_4 \cdot Br^- \rightarrow H_2SO_4 + Br^-$	41.1
$H_2SO_4 \cdot Br^- \rightarrow HSO_4^- + HBr$	27.9

746

747 **Table 3: Calibration coefficients for selected species.**

Species	Calibration coefficient ($molec\ cm^{-3}\ cps\ cps^{-1}$)
I_2	[a] 2.7×10^{10}
I_2	[b] 6.3×10^{10}
Cl_2	[b] 3.5×10^{11}
HOI	[b] 3.3×10^{11}
H_2SO_4	[a] 4.1×10^{10}

748   a: inter-method calibrations

749   b: offline calibrations